



Mechanical behavior of bio-inspired nacre-like composites: A hybrid multiscale modeling approach

Fabrizio Greco^{a,*}, Lorenzo Leonetti^a, Andrea Pranno^{a,b}, Stephan Rudykh^b

^a Department of Civil Engineering, University of Calabria, Rende, Italy

^b College of Engineering, University of Wisconsin-Madison, Madison, WI USA

ARTICLE INFO

Keywords:

Bio-inspired composites
Nacre-like microstructure
Finite deformations
Multiscale models
Nonlinear homogenization
Finite element method

ABSTRACT

In this paper, the mechanical behavior of bio-inspired nacre-like staggered composites is studied. The bio-inspired materials, combining stiff and soft constituents, exhibit superior mechanical properties. Here, the attention is focused on the competing properties: penetration resistance and flexibility of the composites. To this end, a novel hybrid multiscale method is developed, combining a hierarchical multiscale approach with a concurrent approach. The method allows to perform accurate parametric nonlinear analyses at a low computational cost. The influence of the microstructural parameters (i.e., platelet aspect ratio and volume fraction) on the macroscopic mechanical behavior is thus analyzed. Finally, the potential of achieving tailored protective properties and flexibility through microstructural design of the bio-inspired composites is illustrated.

1. Introduction

In the past few years, materials reinforced with fibers, particles or platelets have been increasingly studied to satisfy the escalating requirements of a wide range of composite materials used in many engineering fields [1–7]. These materials, in the form of advanced composites (advanced metal, ceramic or polymer matrix composites), bio-inspired materials (staggered bone-, tooth- or nacre-like composites) and metamaterials (piezoelectric polymers or ceramics, shape memory alloys, electro-active or magneto-active polymers), find application in aerospace, civil construction, automotive, electronic devices, sport goods, furniture and bio-medical equipment. Such materials have been actively investigated delving into new developments and future possibilities since offer enhanced mechanical properties and additional functionalities provided by the strong interaction between a weak material known as matrix and a stiffer material known as reinforcement. Among these, composite materials inspired by biological structures, such as bone and nacre materials [8], are currently the focus of extensive research devoting significant efforts to obtain optimized structural constituents. For instance, a nacre-like composite is usually composed of 95% of high aspect ratio stiff material (in the form of platelets, also referred to as inclusions) and of 5% of soft material in a staggered structure with a brick-and-mortar arrangement, and it exhibits exceptional toughness and strength under tension in the direction parallel to the longitudinal platelet axis but results weak in the

transverse direction [9,10]. Several authors reported that the mechanical properties of nacre-like microstructures are mostly characterized by the interaction between the platelets and that the enhanced mechanical performances are provided by several mechanisms acting on distinct length scales [11]. Consequently, understanding the platelet's interaction and the mechanical properties of the bonding interfaces between soft and stiff phases is necessary to elucidate the microstructure-property relations. This understanding will enable the design of materials with enhanced mechanical properties – including stiffness, toughness, ductility or impact and penetration resistance – through tailored choices of constituent materials and geometrical arrangements. For instance, the sliding resistance of platelets can be increased actuating an interlocking mechanism by changing the waviness of the platelet surfaces [3]. The capability of producing microstructures with a high geometrical complexity – provided by the recent development in the additive manufacturing (AM) or 3D printing – opened new ways for mechanical characterization of bio-inspired composites at different length scales [12]. For instance, a fracture response is analyzed on a biomaterial composite with a bone-like microstructure [13], the performance of a nacre-like composite panel is investigated in terms of deformation and energy dissipation [14], a design strategy of isotropic two-dimensional structural composites consisting of stiff and soft constituents arranged in square, triangular, and quasicrystal lattices is defined [15], a structure created by mimicking fish scale protective system is experimentally tested to reveal its ability to provide

* Corresponding author at. Department of Civil Engineering, University of Calabria, 87036 Rende, Cosenza, Italy.

E-mail address: f.greco@unical.it (F. Greco).

<https://doi.org/10.1016/j.compstruct.2019.111625>

Received 3 October 2019; Accepted 29 October 2019

Available online 31 October 2019

0263-8223/ © 2019 The Authors. Published by Elsevier Ltd. This is an open access article under the CC BY-NC-ND license (<http://creativecommons.org/licenses/by-nc-nd/4.0/>).

protection against penetration while preserving flexibility [16], the overall strength of bio-inspired staggered composites is investigated by employing a micromechanical analysis and by experimental tests on 3D printed composite materials [17], the failure mechanisms of bio-inspired composites subjected to nonaligned loadings is investigated using analytical models and experimental tests [18]. Generally speaking, composite materials, owing to their intrinsic heterogeneities, are commonly afflicted by several nonlinear phenomena especially when they are used in high-performance applications involving a microstructural evolution due to loss of composite integrity (coalescence of micro-cracks, delamination, interface debonding, etc. [19,20]) or to geometrical and/or material nonlinearities induced by large deformations (including micro-buckling and associated microstructure transformations [21–24]). Recent studies reported the influence of nonlinear phenomena on the macroscopic response in undamaged hyperelastic material models [25–31], and the role of interactions between different microscopic failure modes (fracture and instability) [32–36]. Here, we investigate the response in bio-inspired microstructured materials with nonlinear constituents. The task to determine the macroscopic response of microstructured materials taking into account their microscopic mechanical behavior, including microstructural evolution, usually requires a rigorous description of all microstructural details leading to daunting computational efforts. In the past, to overcome direct modeling, several approaches have been proposed in the framework of small and large deformation such as classical homogenization techniques [37–41] and multi-scale strategies [42–46], requiring the development of specialized numerical procedures based on the finite element method. The application of these advanced computational techniques has been mainly reserved for the traditional composite materials, while for the bio-inspired microstructured materials, comprehensive research of the mechanical behavior in large deformation is still limited. Particularly, the optimization of the patterns and dimensions of the components of nacre-like composite microstructures has not been investigated. In the present work, a novel hybrid multiscale strategy is proposed to predict the mechanical behavior of nacre-like composite material in a large deformation context with the purpose of identifying the compromise between penetration resistance and flexibility to design a body protective bio-inspired material architecture. The main idea of the proposed multiscale approach is to combine the advantages of hierarchical and concurrent approaches using a numerical strategy that is able to replace the typical procedure of extracting the homogenized constitutive law for each time step solving a BVP in each Gauss point with a macro-stress/macro-strain database obtained in a pre-processing step. Then, comprehensive parametric analysis with respect to the main microstructural geometrical parameters (platelets aspect ratio and stiff-phase volume fraction), governing the macroscopic behavior of bio-inspired nacre-like composite is performed analyzing its penetration resistance and flexibility. To this end, a material performance metric, the protecto-flexibility, incorporating the performance requirements of penetration resistance and flexibility in one parameter, was analyzed to investigate the role of microstructural parameters in this integrated measure and revealing advantageous microstructured configurations that can be used for design and further optimization of the nacre-like composite material.

2. Numerical framework of the hybrid multiscale approach

Multiscale approaches provide a framework for constructing computational models able to simulate physical systems incorporating more detailed material information and a more complex geometrical structure by examining the behavior of the analyzed system at different length scales. The literature on multiscale modeling shows a variety of approaches, but the focus of recent research has been on hybrid algorithms that somehow combine the standard multiscale methods widely investigated in the past years. These methods are usually categorized as either hierarchical or concurrent. The first ones (see Fig. 1) are the most

commonly used since they are computationally the most efficient, because the response of a representative volume element under prescribed microscopic boundary conditions is determined first over a range of macrostrain loading paths, and from these, a constitutive law is then extracted.

At the end of this procedure, a microscopically informed macroscopic model is obtained, and it can then be used to analyze the macroscopic behavior of the system under different conditions. Function values that are not found in the extracted values can be obtained using interpolation methods. Hierarchical approaches are generally well suited for problems characterized by a weakly coupled relation between different analysis scales; hence application of these techniques on nonlinear mechanical problems presents significant complexities, and in some instances are invalid, in case of damage and failure for example.

The second is characterized by the presence of a fine-scale model linked to the coarse-scale model, such that the coarse-scale model exchanges information directly with the fine-scale model and vice versa through some coupling procedure, as shown in Fig. 2. Both compatibility and momentum balances are enforced across the interface to restore the continuity conditions between the two submodels. Such models are effective when the behavior at each scale depends strongly on what happens at the other scale.

In this work, a hybrid hierarchical/concurrent multiscale approach (see Fig. 3) is proposed with the main idea to combine the advantages of the hierarchical and of the concurrent approach through a numerical strategy able to further reduce the computational effort required by the concurrent multiscale approaches already investigated by other authors [47,48]. In general terms, the hybrid multiscale analysis can be performed identifying the area domains in which a fine scale modeling must be used to capture the resulting high effect of all the nonlinearities (material, geometrical, damage, friction, etc.), and the area domains in which a coarse scale can be used.

The fine-scale domain is characterized by a microstructural evolution which requires a numerical model able to describe all its microscopic details completely and may contain heterogeneities, singularities, defects or some other notable geometrical or material nonlinearities leading to a more considerable computational effort. A homogeneous continuum model, instead, uses information obtained by a representative volume element (RVE) at the fine scale to describe the mechanical behavior of the homogenized material characterizing the coarse-scale domain. Specifically, the typical procedure to solve a boundary value problem (BVP) on the RVE in each Gauss point and for each time step of the macroscopic simulation (in the spirit of the classical FE2 method), has been now replaced with the application of a macro-stress/macro-strain database previously extracted. Thus, a database and an interpolation method are used to obtain the macro-stress of the homogenized model. In this hybrid approach the following steps have to be performed:

- i) identification of an RVE whose individual constituents are assumed to be known entirely, together with their constitutive properties;
- ii) formulation of the microscopic boundary conditions to be applied to the RVE;
- iii) solving the BVP for a given macroscopic strain path, the average stress and strain are calculated;
- iv) step iii is repeated in order to create a numerical data point in the macroscopic gradient tensor space, in which radial strain paths are parametrized by using spherical coordinates; the average of the stress and the strain is evaluated for every time step and stored in a database matching the information on strains with information on stresses;
- v) after the previous steps are performed, the obtained constitutive law in the form of strain/stress database is incorporated in the computational model together with an interpolation method able to give as output not only the interpolated values of the stresses, but

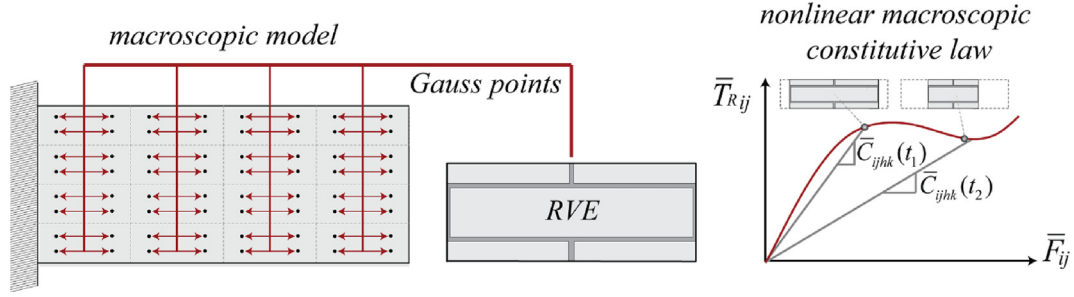


Fig. 1. Schematic representation of the hierarchical multiscale approach.

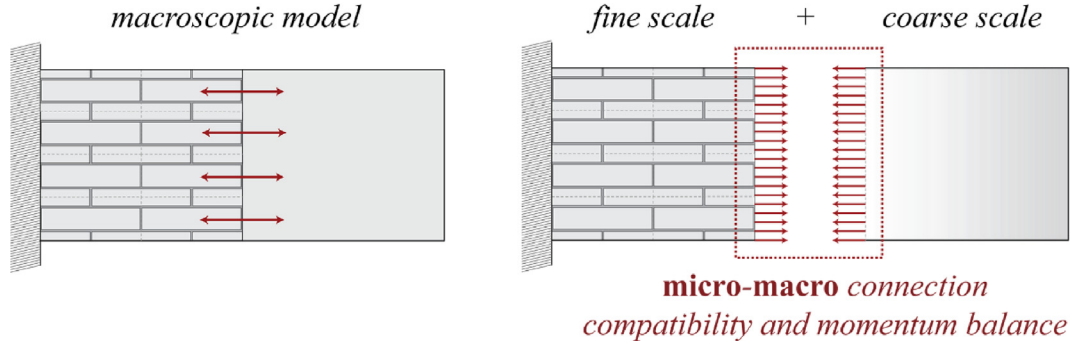


Fig. 2. Schematic representation of the concurrent multiscale approach.

also the derivative of the interpolated function (useful to evaluate the tangent stiffness matrix);

- vi) at the end, the fine and the coarse scale are joined together in a macroscopic model obtaining a substantial reduction of the computational effort compared to a full-scale direct analysis (DNS).

3. Theoretical background of the RVE problem in a large deformation context

To describe finite deformation of a continuous body, we introduce the position vectors \mathbf{X} and \mathbf{x} , corresponding to the reference (undeformed) and deformed configuration, respectively. Each point of the undeformed configuration at the time t , has position \mathbf{x} given by $\mathbf{x} = \mathbf{x}(\mathbf{X}, t)$. The relation between \mathbf{X} and \mathbf{x} is defined by $\mathbf{x}(\mathbf{X}, t) = \mathbf{u}(\mathbf{X}, t) + \mathbf{X}$ in which $\mathbf{u}(\mathbf{X}, t)$ is the displacement vector field and the deformation gradient tensor is defined as $\mathbf{F}(\mathbf{X}, t) = \partial \mathbf{x}(\mathbf{X}) / \partial \mathbf{X}$. Then, the Jacobian $J \equiv \det \mathbf{F}$ defines the volume change of the body with respect to the reference configuration. The constitutive behavior of a hyperelastic material can be described in terms of an objective strain energy-density function $W(\mathbf{X}, \mathbf{F})$ and hence, the first Piola-Kirchhoff stress tensor can be defined as

$$\mathbf{T}_R = \frac{\partial W(\mathbf{X}, \mathbf{F})}{\partial \mathbf{F}}. \quad (1)$$

The corresponding Cauchy stress tensor and second Piola-Kirchhoff stress tensor are related to the first Piola-Kirchhoff stress tensor via $\boldsymbol{\sigma} = J^{-1} \mathbf{T}_R \mathbf{F}^T$ and $\mathbf{T}^{(2)} = \mathbf{F}^{-1} \mathbf{T}_R$, respectively. For a neo-Hookean material, the strain energy function is given as

$$W(\mathbf{F}) = \frac{1}{2} \mu (I_1 - 3) - \mu \ln(J) + \frac{1}{2} \lambda [\ln(J)]^2, \quad (2)$$

where μ is the shear modulus of the material, $I_1 = \text{tr}(\mathbf{C})$ is the first invariant of the right Cauchy-Green deformation tensor $\mathbf{C} = \mathbf{F}^T \mathbf{F}$, λ is the first Lamé parameter that is related to the bulk modulus k (modulus of compressibility) and to the shear modulus. Considering deformation applied quasi-statically and the absence of body forces, the equation of motion can be written in the undeformed configuration as

$$\text{Div } \mathbf{T}_R = \mathbf{0}. \quad (3)$$

Then, the homogenization problem for a heterogeneous solid (steps i, ii and iii), whose periodic microstructure consists of stiff rectangular platelets separated by thin layers of soft material (bio-inspired nacre-like composite material) is formulated in the following. The microstructural equilibrium problem is here formulated in terms of the deformation gradient \mathbf{F} and of its conjugate stress measure \mathbf{T}_R because is

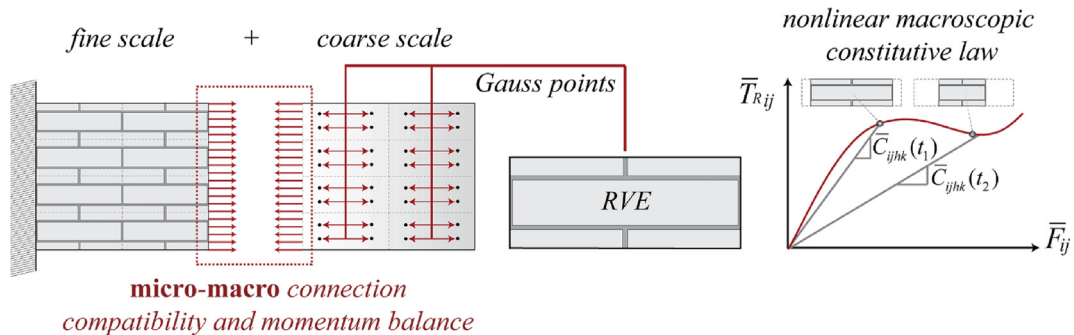


Fig. 3. Schematic representation of the hybrid hierarchical/concurrent multiscale approach.

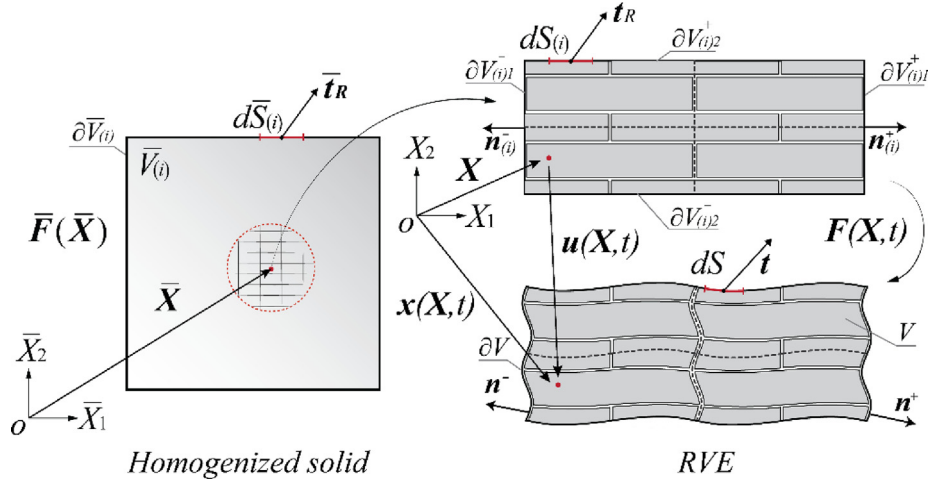


Fig. 4. 2D Representation of the homogenized solid of a staggered composite material (on the left) and of its corresponding undeformed and deformed RVE configurations (on the right) attached to a generic macroscopic material point in the X_1 - X_2 plane.

convenient in defining the essential boundary conditions (BCs) on the unit cell. With reference to Fig. 4, the volume of the homogenized solid denoted by $\bar{V}_{(i)}$ in the undeformed reference configuration is enclosed by the surface $\partial\bar{V}_{(i)}$, on which the first Piola-Kirchhoff traction vector $\bar{\mathbf{t}}_R$ acts (note that the subscript (i) is referred to variables in the initial configuration).

The RVE is assumed to be associated with an infinitesimal neighborhood of a generic macroscopic material point $\bar{\mathbf{X}}$. Each microstructural constituent is characterized by an incrementally linear relationship between the first Piola-Kirchhoff stress rate tensor $\dot{\mathbf{T}}_R$ and the deformation gradient rate tensor $\dot{\mathbf{F}}$ as follow: $\dot{\mathbf{T}}_R = \mathbf{C}^R(\mathbf{X}, \mathbf{F})[\dot{\mathbf{F}}]$ in which $\mathbf{C}^R(\mathbf{X}, \mathbf{F})$ is the fourth-order tensor of nominal moduli satisfying the major symmetry condition ($C^{R}_{ijkl} = C^{R}_{klij}$). This constitutive law is representative of a large class of rate-independent materials (including hyperelastic ones), and every loading process can be parametrized in terms of a time-like parameter $t \geq 0$ monotonically increasing ($t = 0$ in the undeformed configuration). The rates of field quantities are evaluated as the derivatives with respect the parameter t that describes the quasi-static deformation path of the composite solid. The micro- and macro-scales can be coupled by the common relations that define the macroscopic first Piola-Kirchhoff stress tensor $\bar{\mathbf{T}}_R$ and the macroscopic deformation gradient $\bar{\mathbf{F}}$ as a function of boundary data of the traction field \mathbf{t}_R and of the deformation field $\mathbf{x}(\mathbf{X}, t)$, respectively:

$$\bar{\mathbf{T}}_R(t) = \frac{1}{|\bar{V}_{(i)}|} \int_{\partial\bar{V}_{(i)}} \mathbf{t}_R(\mathbf{X}, t) \otimes \mathbf{X} dS_{(i)}, \quad \bar{\mathbf{F}}(t) = \frac{1}{|\bar{V}_{(i)}|} \int_{\partial\bar{V}_{(i)}} \mathbf{x}(\mathbf{X}, t) \otimes \mathbf{n}_{(i)} dS_{(i)}, \quad (4)$$

in which \otimes denotes the tensor product, $\mathbf{n}_{(i)}$ the outward normal at $\mathbf{X} \in \partial V_{(i)}$ and $\mathbf{t}_R = \mathbf{T}_R \mathbf{n}_{(i)}$ the nominal traction vector. In a macrostrain-driven loading regime is assumed that the microscopic deformation field can be additively split into a linear part and a fluctuating part:

$$\mathbf{x}(\mathbf{X}, t) = \bar{\mathbf{F}}(t)\mathbf{X} + \mathbf{w}(\mathbf{X}, t), \quad (5)$$

where $\bar{\mathbf{F}}(t)\mathbf{X}$ is a linear displacement contribution and $\mathbf{w}(\mathbf{X}, t)$ is the fluctuation field. Inserting the definition of the microscopic deformation field into the definition of the macroscopic deformation field, it provides an integral constraint that a microscopic displacement fluctuation field should satisfy to be kinematically admissible:

$$\int_{\partial V_{(i)}} \mathbf{w} \otimes \mathbf{n}_{(i)} dS_{(i)} = \mathbf{0}. \quad (6)$$

Then the macro-micro transition is achieved by imposing the appropriate boundary condition on the RVE displacement fluctuation field. Hence, in accordance with the periodic nature of the staggered

composite microstructure, periodic boundary displacement fluctuations can be imposed on the boundaries $\partial V_{(i)}$ of the RVE satisfying the previously mentioned integral constraint:

$$\mathbf{w}(\mathbf{X}^+, t) = \mathbf{w}(\mathbf{X}^-, t) \text{ on } \partial V_{(i)}, \quad (7)$$

where the superscripts + and - denote pairs of opposite RVE boundary points. The imposed periodicity conditions are written as

$$\mathbf{T}_R \mathbf{n}_{(i)}(\mathbf{X}^+, t) = -\mathbf{T}_R \mathbf{n}_{(i)}(\mathbf{X}^-, t) \text{ on } \partial V_{(i)}, \quad (8)$$

$$\mathbf{x}(\mathbf{X}^+, t) - \mathbf{x}(\mathbf{X}^-, t) = \bar{\mathbf{F}}(t)(\mathbf{X}^+ - \mathbf{X}^-) \text{ on } \partial V_{(i)}, \quad (9)$$

representing antiperiodic traction (8) and periodic deformation (9) imposed on the boundary of the RVE. Finally, the equilibrium boundary value problem at given macrodeformation gradient is governed by the following equations:

$$\begin{cases} \text{Div } \mathbf{T}_R = \mathbf{0} & \text{in } V_{(i)} \\ \mathbf{T}_R \mathbf{n}_{(i)}(\mathbf{X}^+, t) = -\mathbf{T}_R \mathbf{n}_{(i)}(\mathbf{X}^-, t) & \text{on } \partial V_{(i)} \end{cases} \quad (10)$$

Solving this boundary value problem, the macroscopic constitutive quantities that are essential to proceed with the stress-strain database determination can then be extracted by applying appropriate volume averages (4). The macroscopic constitutive response, in terms of the homogenized tangent moduli tensor $\bar{\mathbf{C}}^R(\bar{\mathbf{F}})$, can be expressed as a function of the microscopic tangent moduli tensor $\mathbf{C}^R(\mathbf{X}, \bar{\mathbf{F}})$ as follows:

$$\bar{\mathbf{C}}^R_{ijkl}(\bar{\mathbf{F}}) = \frac{1}{|\bar{V}_{(i)}|} \int_{V_{(i)}} \mathbf{C}^R_{ijmn}(\mathbf{X}, \bar{\mathbf{F}}) [I^{hk}_{mn} + \nabla w^{hk}_{mn}] dV_{(i)}, \quad (11)$$

where \mathbf{w}^{hk} denotes the incremental fluctuation field induced by $\dot{\bar{\mathbf{F}}} = \mathbf{I}^{hk}$.

4. Macro-stress/macro-strain database determination

In this section, more detailed information about the procedure adopted to extract the macro-stress/macro-strain database is given (step iv). The strategy adopted to parameterize the radial loading paths by using spherical coordinates is based on the space of the macroscopic right stretch tensor ($\bar{\mathbf{U}}$) instead of on the space of the macroscopic deformation gradient tensor ($\bar{\mathbf{F}}$); this allows to significantly decrease the computational effort requested for the creation of the database. As a matter of fact, in a planar setting, $\bar{\mathbf{F}}$ is described by a 2×2 matrix whose components are: \bar{F}_{11} , \bar{F}_{12} , \bar{F}_{21} and \bar{F}_{22} , hence a numerical data point database must be represented on a four-dimensional space leading to an expensive computationally effort with respect to a parameterization on a three-dimensional space. The adopted procedure to

overcome this complexity exploits the objectivity of the macroscopic strain energy function \bar{W} by means of the following relation [49]:

$$\bar{W}(\bar{\mathbf{Q}}\bar{\mathbf{F}}) = W(\bar{\mathbf{F}}) \quad \forall \bar{\mathbf{Q}} \in \text{Orth}^+, \quad (12)$$

where \bar{W} is defined as:

$$\bar{W} = \frac{1}{|V_{(i)}|} \int_{V_{(i)}} W(\mathbf{X}, \bar{\mathbf{F}}) dV_{(i)}, \quad (13)$$

and $\bar{\mathbf{Q}}$ is an arbitrary proper orthogonal tensor. Eq. (12) is a direct consequence of the assumed objectivity of W and leads to the following reduced form of the constitutive law:

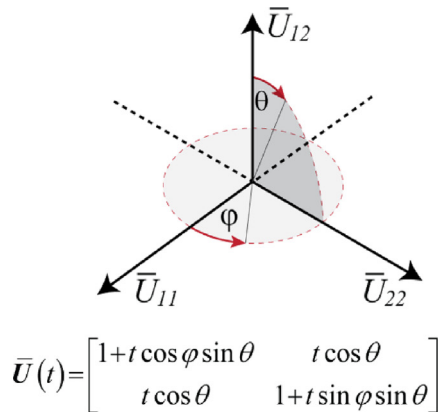
$$\bar{\mathbf{T}}_R(\bar{\mathbf{F}}) = \bar{\mathbf{R}}\bar{\mathbf{T}}'_R(\bar{\mathbf{U}}), \quad (14)$$

where $\bar{\mathbf{T}}'_R$ is the restriction of $\bar{\mathbf{T}}_R(\bar{\mathbf{F}})$ to positive-definite symmetric tensors ($Psym$), $\bar{\mathbf{U}}$ is the macroscopic right stretch tensor involved with the polar decomposition $\bar{\mathbf{F}} = \bar{\mathbf{R}}\bar{\mathbf{U}}$ and $\bar{\mathbf{R}}$ is the macroscopic rotation tensor. Eq. (14) states that the constitutive properties of the homogenized material are not influenced by the rotational part of the macrodeformation $\bar{\mathbf{R}}$. Since the response function $\bar{\mathbf{T}}_R(\bar{\mathbf{F}})$ is completely determined by its restriction to positive-definite symmetric tensors, during the database creation phase we can assume that $\bar{\mathbf{R}} = \mathbf{I}$ and $\bar{\mathbf{F}} = \bar{\mathbf{U}}$ in order to determine the restricted response function $\bar{\mathbf{T}}'_R(\bar{\mathbf{U}})$. Definitely, since $\bar{\mathbf{U}}$ is a 2×2 symmetric matrix with components \bar{U}_{11} , $\bar{U}_{12} = \bar{U}_{21}$ and \bar{U}_{22} , we can parameterize the restricted homogenized response function using spherical coordinates (see Fig. 5) in a three-dimensional space with axes representing the components of $\bar{\mathbf{U}}$.

The 3D space is scanned fixing the radial direction (by varying θ from 0° to 180° and φ from 0° to 360°) and incrementing the time-like parameter t , therefore each database point corresponding to the macroscopic first Piola-Kirchhoff stress is evaluated in a time step t of the imposed radial loading path. The homogenized constitutive law can be hence extracted by imposing a sufficient number of radial loading paths and an adequate time step to store as much information as possible about the response of the RVE in every load direction. This procedure was implemented in the finite element code COMSOL 5.4 integrating, via a MATLAB script, a parametric sweep to allow θ and φ to be swept through a prefixed range of values. Once the database is created, an additional step is necessary because the variational formulation of the adopted numerical environment is written in terms of the second Piola-Kirchhoff stress ($\bar{\mathbf{T}}^{(2)} = \bar{\mathbf{F}}^{-1}\bar{\mathbf{T}}_R$) and the Green-Lagrange strain ($\bar{\mathbf{E}} = (\bar{\mathbf{F}}^T\bar{\mathbf{F}} - \mathbf{I})/2$) as frame-indifferent work-conjugate stress-strain pair. For this reason, the previously discussed database function of $\bar{\mathbf{U}}(t)$ and $\bar{\mathbf{T}}'_R(\bar{\mathbf{U}}(t))$ must be transformed using the following relations:

$$\bar{\mathbf{E}} = \frac{1}{2}(\bar{\mathbf{U}}^2 - \mathbf{I}), \quad (15)$$

$$\bar{\mathbf{T}}^{(2)} = \bar{\mathbf{U}}^{-1}\bar{\mathbf{T}}'_R, \quad (16)$$



leading to a work-conjugated stress/strain database function of $\bar{\mathbf{E}}$ and $\bar{\mathbf{T}}^{(2)}$. Once the restricted response function database is built, the macroscopic constitutive response to a generic macrodeformation point can be obtained by applying Eq. (14). In addition, the obtained macroscopic stress will be used to compute the tangent constitutive matrix by using the following relation:

$$\bar{\mathbf{C}}^{(2)} = \frac{\partial \bar{\mathbf{T}}^{(2)}}{\partial \bar{\mathbf{E}}}, \quad (17)$$

where $\partial \bar{\mathbf{T}}^{(2)}/\partial \bar{\mathbf{E}}$ is a fourth-order tensor whose component are $\bar{\mathbf{C}}^{(2)}_{ijkl} = \partial \bar{\mathbf{T}}^{(2)}_{ij}/\partial \bar{\mathbf{E}}_{kl}$. The macro-stress/macro-strain database is implemented by means of an external material routine that allows defining the homogenized material model in the macroscopic domain. A linear interpolation function is recalled inside the external material routine to interpolate the macro-stress/macro-strain database loaded as unstructured file data in which the values of the function are matched in a discrete generic point cloud. A Newton-Raphson solver is employed to find the solution of the nonlinear macroscopic problem and, during Newton-Raphson iterations, the external material routine is recalled for each Gauss point until the solution was converged to within the desired tolerance.

5. Numerical applications

The multiscale analysis technique described in Section 2 is here applied to analyze the penetration resistance and the flexibility of bio-inspired composites with nacre-like microstructure. The periodic unit cell shown in Fig. 6 describes the investigated representative volume element, containing hard platelets connected by soft matrix materials and arranged in an overlapping brick-and-mortar pattern.

The thickness of the matrix interphase is denoted with H_i , H and L denote the height and the length of the unit cell respectively, H_p and L_p denote the height and the length of platelets. With reference to [17], since linear elastic model can provide adequate approximation for material behavior for small strains (typically not exceeding 5%), the stiff platelets are modeled as linear elastic material with elastic modulus $E_p = 1.8$ GPa and Poisson's ratio $\nu = 0.42$, while the soft interphase is modeled as nearly incompressible neo-Hookean material with initial shear modulus $\mu_i = 0.21$ MPa (a bulk modulus equal to $1000\mu_i$ is adopted to simulate the incompressibility condition). The length of the platelets is $L_p = 20$ mm, the amount of hard inclusions in a unit cell is defined by $v_f = \frac{(L_p H_p)}{(L_p + H_i)(H_p + H_i)}$ and the platelets aspect ratio is defined by $w = \frac{L_p}{H_p}$. Multiscale parametric analyses were performed to analyze the influence of the platelets volume fraction and the platelets aspect ratio on the flexibility and on the penetration resistance by varying the main microstructural geometrical parameters (v_f and w) with reference to the

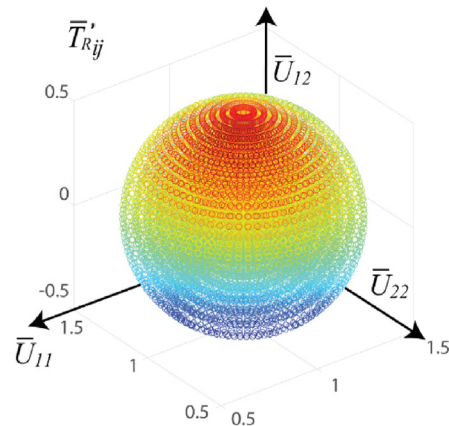


Fig. 5. 3D space of right stretch tensors parametrized using spherical coordinates (on the left) and an example of MATLAB scattered plot of the stress tensor extracted from a 3D reduced database obtained.

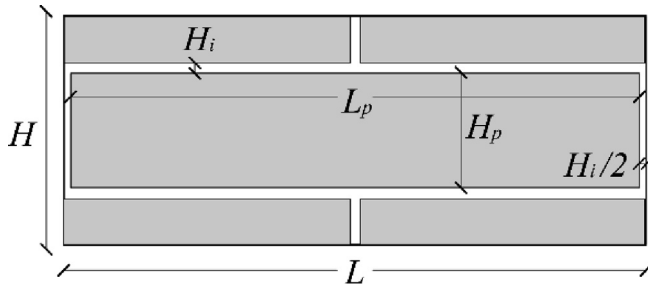


Fig. 6. 2-D Periodic microgeometrical arrangement of bio-inspired nacre-like composite. The gray and white areas represent the hard inclusions (platelets) and the soft interphase (matrix) respectively.

above described microstructure.

The flexibility was investigated employing a three-point bending test on beams composed by a 14×4 unit cell assembly (column \times row), as shown in Fig. 7a, in which the real microstructure is introduced only in correspondence of the vertical concentrated load where the local effects are more intense. The penetration resistance was investigated employing an indentation test on a rectangular sample composed by a 6×4 unit cell assembly using a spherical indenter with radius equal to $L/4$, as shown in Fig. 7b.

Numerical simulations were performed using the finite element code COMSOL 5.4 considering a 2D system in plane-strain conditions applying displacement-controlled loadings in a quasi-static regime. The typical mesh adopted for the examined unit cell is of a structured type and involves quadratic Lagrangian quadrilateral elements. The contact condition between the indenter and the sample was modeled by a penalty method which is rather simple and robust, based on inserting a stiff spring bed, active only in compression, between the contacting boundaries. First of all, validation and mesh convergence tests of the multiscale model were reported comparing numerical results obtained by means of a multiscale numerical simulation (MNS) with numerical results obtained by means of a direct numerical simulation (DNS) in which the composite microstructure is explicitly modeled.

As shown in Fig. 8a and b both the multiscale models give a slightly stiffer response (with respect to the DNS simulations) and a higher influence of the degrees of freedom on the response is observed for the indentation test simulations. Anyway, for both the examined tests, no more than 20,000 degrees of freedom are needed for the multiscale approach to obtain a response in good agreement with the direct model results, thus saving between 50 and 60% of computational effort required for a full-scale direct numerical analysis.

5.1. Numerical investigation of the flexibility property

With reference to the three-point bending test, the dependence of the normalized bending load on the bending angle for nacre-like composite structures with inclusions volume fraction ranging from 0.5 to 0.9 with increments of 0.1, and platelets aspect ratio ranging from 6 to 10 with increments of 2, is shown in Fig. 9. The normalized bending load is defined as $M = \frac{FL_s}{\mu_i H_{tot} H_p z}$, where L_s is the distance between the supports, H_{tot} is the total height of the beam and z is the out-of-plane depth, while the bending angle is defined as $\alpha = \text{atan}\left(\frac{2\delta}{L_{tot}}\right)$ where δ is

the vertical displacement in the middle of the beam and L_{tot} is the total length of the beam. The flexibility decreases with an increase in volume fraction, as well as with an increase in aspect ratio. Nacre-like microstructures with volume fraction equal to 0.9 (green lines) results in a more pronounced decrease of flexibility leading, for instance, to values of the normalized load approximately doubled with respect to arrangements with volume fraction equal to 0.8 (fuchsia lines), at fixed inclusions aspect ratio.

The composite flexibility is further investigated by plotting the relative bending stiffness as function of aspect ratio in Fig. 10a and volume fraction in Fig. 10b. The relative bending stiffness represents a non-dimensional bending stiffness taken as the tangent bending stiffness of the composite beam divided by the tangent bending stiffness of the homogeneous beam ($v_f = 0$). Since the relative bending stiffness changes with bending angle, the initial tangent stiffness (measured at $\alpha = 1^\circ$) and the finite tangent stiffness ($\alpha = 15^\circ$) were plotted. The initial stiffness is presented by filled symbols, while the finite stiffness is denoted by hollow symbols. The results show that both initial and finite stiffness increase with an increase in both aspect ratio and volume fraction. In particular, an almost linear dependence on the aspect ratio at fixed volume fraction (Fig. 10a), and a superlinear dependence on the volume fraction at fixed aspect ratio (Fig. 10b) are reported. In other words, the investigated microstructure shows a more pronounced stiffening effect with increasing volume fraction, especially for the finite stiffness values. On the contrary, as shown in Fig. 10a, the aspect ratio has a small effect on the bending stiffness (especially for the initial values), which becomes negligible for low volume fractions (v_f ranging between 0.5 and 0.6). Furthermore, the difference between the finite and initial bending stiffness increases for increasing values of both volume fraction and aspect ratio, and becomes negligible for low volume fractions regardless the considered aspect ratio, meaning that the bending behavior of the given microstructure is nearly linear in these cases (see Fig. 10b).

5.2. Numerical investigation of the penetration resistance property

The dependence of the normalized indentation load on the normalized indentation depth with an inclusions volume fraction ranging from 0.5 to 0.9 with increments of 0.1, and a platelets aspect ratio ranging from 6 to 10 with increments of 2 is shown in Fig. 11. The normalized indentation load is defined as $P = \frac{F}{\mu_i H_{tot} z}$, which is plotted as function of the normalized indentation depth $\Delta = \frac{\delta}{H_{tot}}$ where δ is the vertical displacement at the top of the midsection, coinciding with the central point of the contact area with the indenter. The indentation load levels increase with an increase in inclusions volume fraction, while the aspect ratio provides a slight influence on the indentation load levels. The penetration stiffness increases with increasing indentation depth, as will be shown in more detail next. High volume fractions and low aspect ratios offer the greatest penetration resistance, with the exception of the case with $v_f = 0.9$ (green line), which shows the highest penetration resistance offered with $w = 10$ for levels of the normalized indentation depth greater than 0.12. The influence of the inclusions volume fraction and aspect ratio on the material resistance against indentation is further analyzed by plotting the relative penetration stiffness as function of these parameters in Fig. 12.

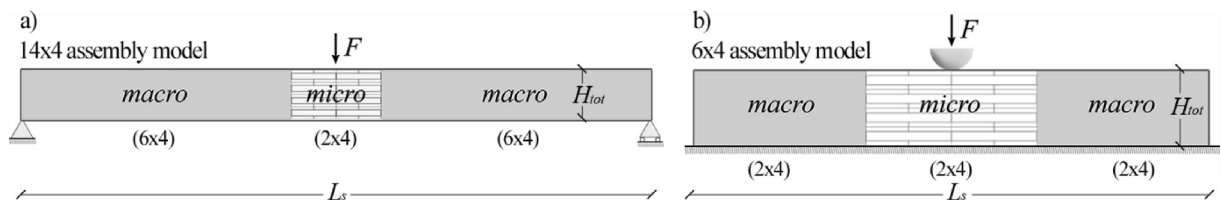


Fig. 7. Schematic of the geometric multiscale models adopted to simulate numerically the three-point bending test (a) and the indentation test (b).

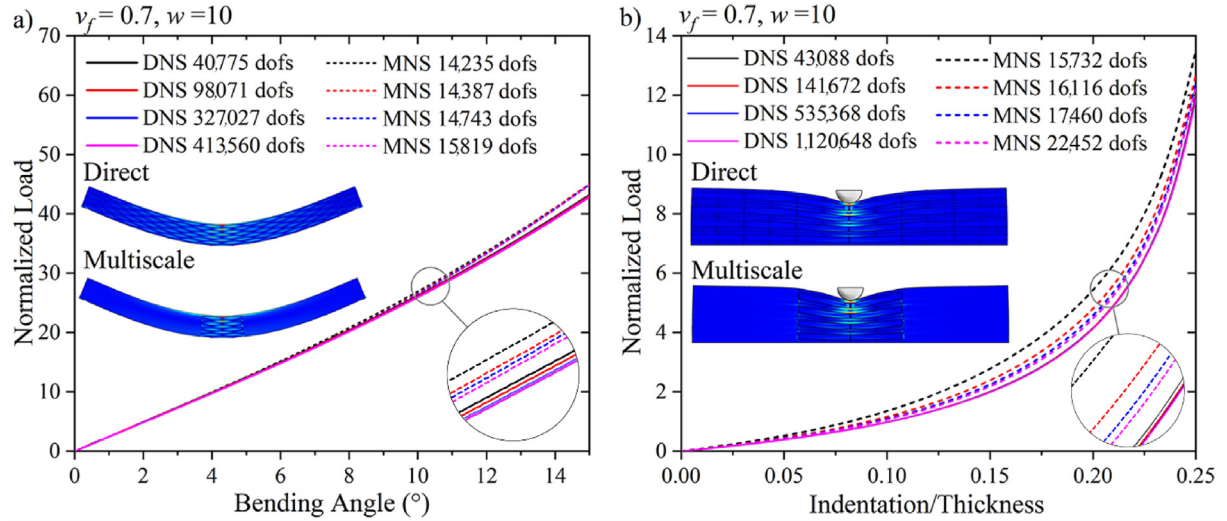


Fig. 8. Normalized bending load vs. bending angle (a) and normalized indentation load vs. normalized indentation depth (b) for nacre-like composite structures with different mesh size using direct (DNS) and multiscale (MNS) numerical simulations.

The relative penetration stiffness is defined here as the tangent penetration stiffness of the composite sample normalized to the tangent penetration stiffness of the homogeneous sample ($v_f = 0$). Since the relative penetration stiffness changes with depth indentation, the initial tangent stiffness is measured at $\Delta = 0.01$ and the finite tangent stiffness is measured at when the tangent stiffness approaches a limit constant value (this occurs generally for the last value of Δ before convergence problems appear).

As in the previous analyzed case, both initial and finite penetration stiffness increase with increasing volume fraction. Moreover, the finite penetration stiffness is much higher than the initial value reflecting the highly nonlinear behavior due to a combination of geometrical and material nonlinearity, mostly for high values of volume fraction (see Fig. 12c and d). The aspect ratio provides a relatively small influence on both the initial and the final penetration stiffness. In detail, the finite penetration stiffness increases with increasing aspect ratio for volume fraction values ranging from 0.5 to 0.7, while decreases for volume fraction equal to 0.8 and 0.9. Consistent with the previous observation, Fig. 12d shows that merely for the cases with $v_f = 0.8$ and 0.9 the maximum value of finite relative penetration stiffness is given by the highest value of aspect ratio ($w = 10$).

5.3. Numerical investigation of the combined protecto-flexibility property

To better investigate the flexibility and the penetration stiffness in a coupled manner, the relative bending stiffness was plotted as function of the relative penetration stiffness in Fig. 13a and b, showing that an increase in penetration protection is accompanied by an increase in bending stiffness (decrease in flexibility) except for the finite relative bending stiffness with $v_f < 0.8$.

In particular, with $v_f = 0.5$ and 0.6, the finite relative bending stiffness can be varied without affecting the finite relative penetration stiffness, which is however negligible with respect to higher volume fractions (see black and red points of Fig. 13b). Fig. 13 clearly shows that the volume fraction strongly influences the penetration stiffness (both initial and finite values) while slightly affecting the bending stiffness, especially for higher values of v_f . Moreover, it can be seen that the aspect ratio influences scarcely the initial penetration stiffness (see Fig. 13a) while influencing moderately both the finite penetration and bending stiffness, except with $v_f < 0.7$, for which no significant influence is reported (see Fig. 13b). These figures also show that the penetration resistance can be tailored as a function of the flexibility properties by opportunely varying the examined microstructural

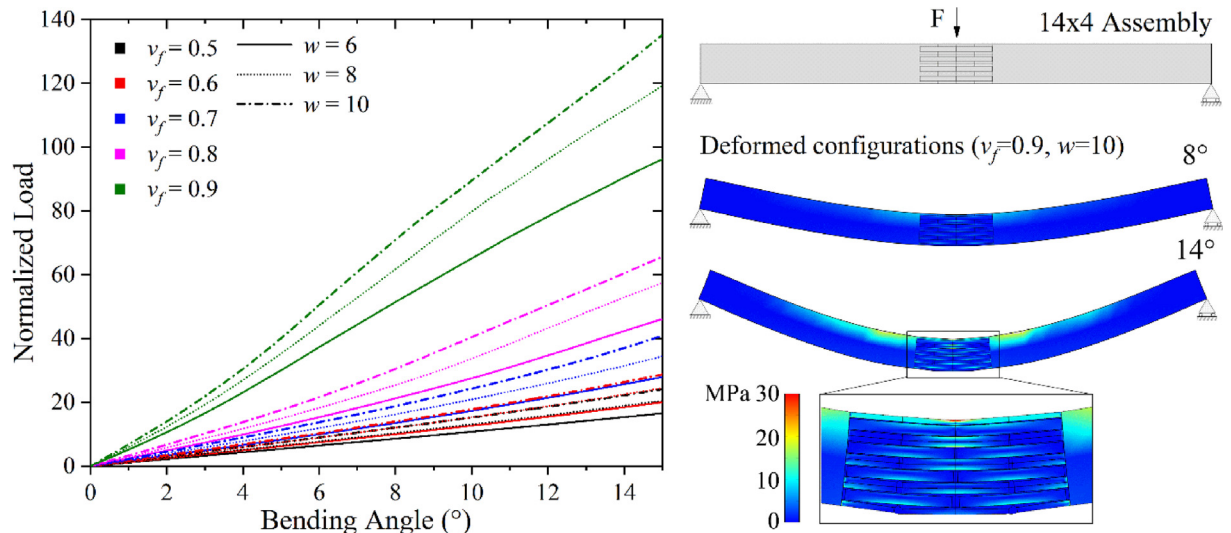


Fig. 9. Normalized bending load vs. bending angle for nacre-like composite structures considering an inclusions volume fraction ranging from 0.5 to 0.9 with increments of 0.1, and an inclusions aspect ratio ranging from 6 to 10 with increments of 2.

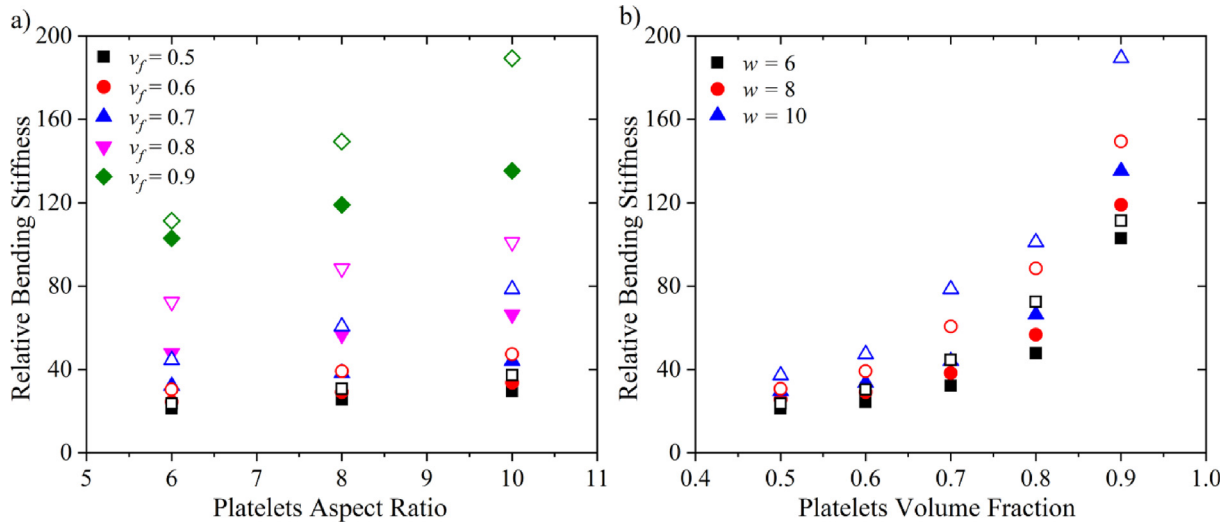


Fig. 10. Relative bending stiffness vs. platelets aspect ratio a) and platelets volume fraction b). The solid and hollow symbols are for initial and finite relative bending stiffness, respectively.

geometrical parameters. In particular, Fig. 13b shows that different combinations of v_f and w may lead to the similar values of the desired finite flexibility and penetration resistance. In particular, once the desired finite relative bending stiffness is assigned to the nacre-like material, the volume fraction and the platelets aspect ratio can be optimized such that the desired relative penetration stiffness is reached. For instance, after choosing a finite relative bending stiffness of about 100, a finite relative penetration stiffness ranging between 3500 and 4500 can be achieved either for $v_f = 0.8$ and $w > 10$ or for $v_f = 0.9$ and $w < 6$.

Then, the contrasting combination of penetration protection and flexibility, called protecto-flexibility, was taken as the ratio $\Omega = C_p/C_B$ between the normalized indentation stiffness C_p and the normalized bending stiffness C_B . The influence of the microstructural geometry of the composite on Ω is shown in Fig. 14, in which Ω is plotted as function of aspect ratio (a, b) and volume fraction (c, d). This figure clearly shows that the protecto-flexibility increases with increasing volume fraction and decreasing aspect ratio except for the cases with $v_f = 0.9$ and $w = 8, 10$, shown in Fig. 14d, where Ω is lower compared to the cases with $v_f = 0.8$ and $w = 8, 10$. Note that the finite protecto-

flexibility is very sensitive to changes in volume fraction and aspect ratio, on the contrary, the initial protecto-flexibility does not change significantly with a change in volume fraction or aspect ratio. We can observe that volume fractions of 0.8 and 0.9 are optimal to achieve the best combinations of flexibility and penetration resistance. Considering the initial protecto-flexibility, we can see that, for each fixed aspect ratio, the highest value is obtained for $v_f = 0.9$ as shown in Fig. 14a; on the other hand, at finite deformations, the highest value, of about 40, is obtained for $v_f = 0.9$ and $w = 6$. For this value of aspect ratio, the general trend is that increasing value of the volume fraction are associated with increasing value of the protecto-flexibility. Such a trend is not reported for higher aspect ratios, i.e. $w = 8$ and 10 , where the optimal value of the volume fraction to achieve the highest protecto-flexibility is $v_f = 0.8$. Finally, it is worth noting that the finite protecto-flexibility is more important, being in general two orders of magnitude greater than the initial one. This means that the protecto-flexibility properties appear in the considered staggered nacre-like material only at large deformation, essentially due to the delayed activation of the penetration stiffness.

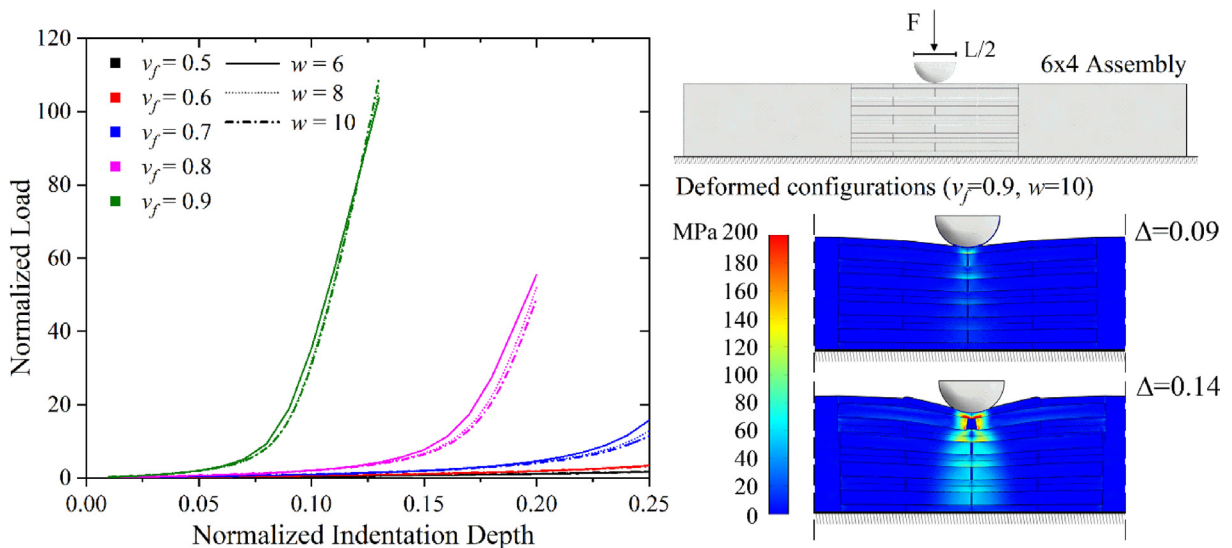


Fig. 11. Normalized indentation load vs. normalized indentation depth for nacre-like microstructures considering an inclusions volume fraction ranging from 0.5 to 0.9 with increments of 0.1, and a platelets aspect ratio ranging from 6 to 10 with increments of 2.

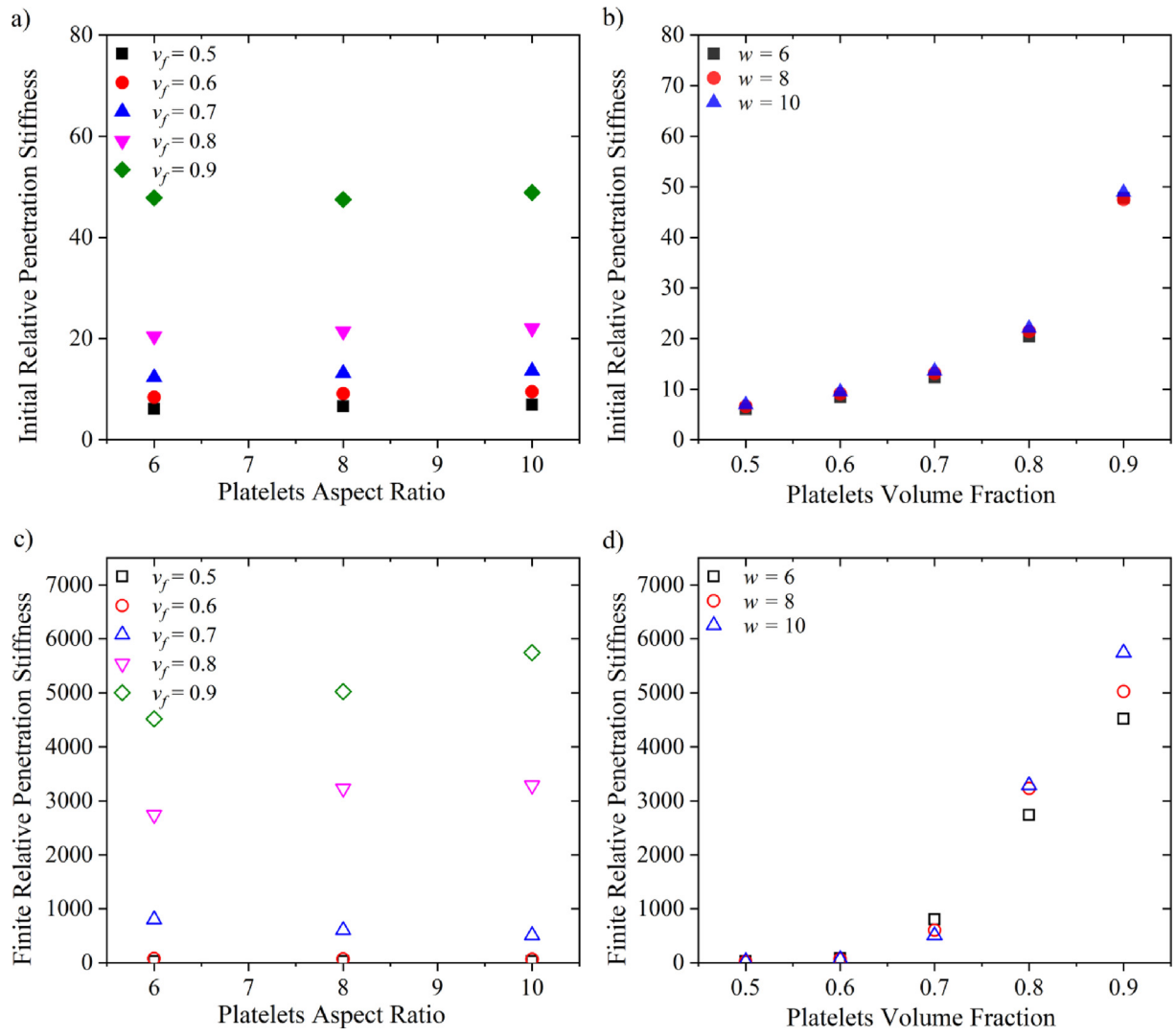


Fig. 12. Relative penetration stiffness vs. platelets aspect ratio: a) initial and c) finite values. Relative penetration stiffness vs. platelets volume fraction: b) initial and d) finite values.

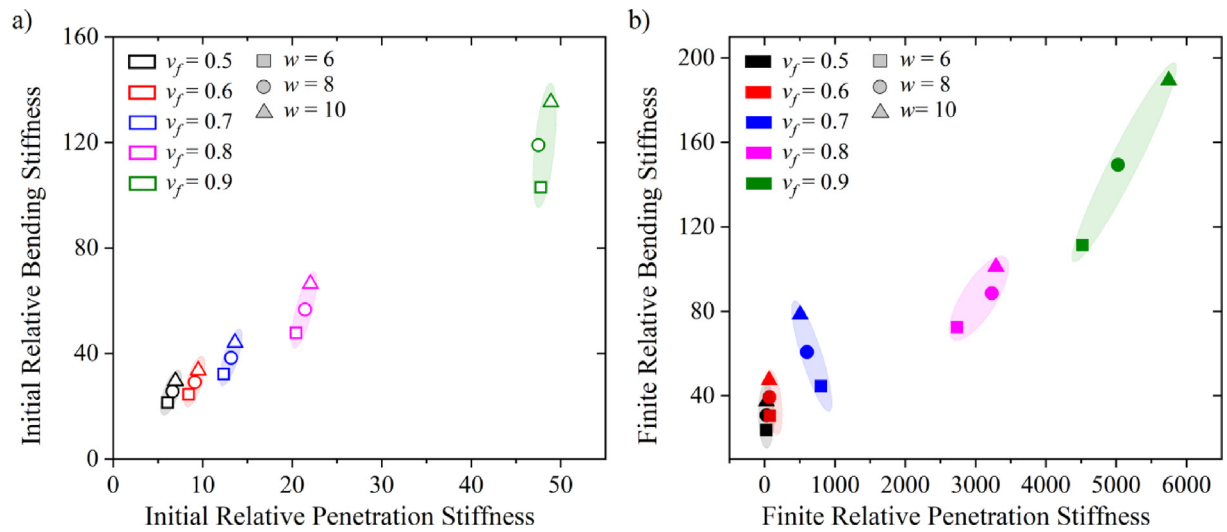


Fig. 13. Relative bending stiffness vs. relative penetration stiffness: a) initial and b) finite values.

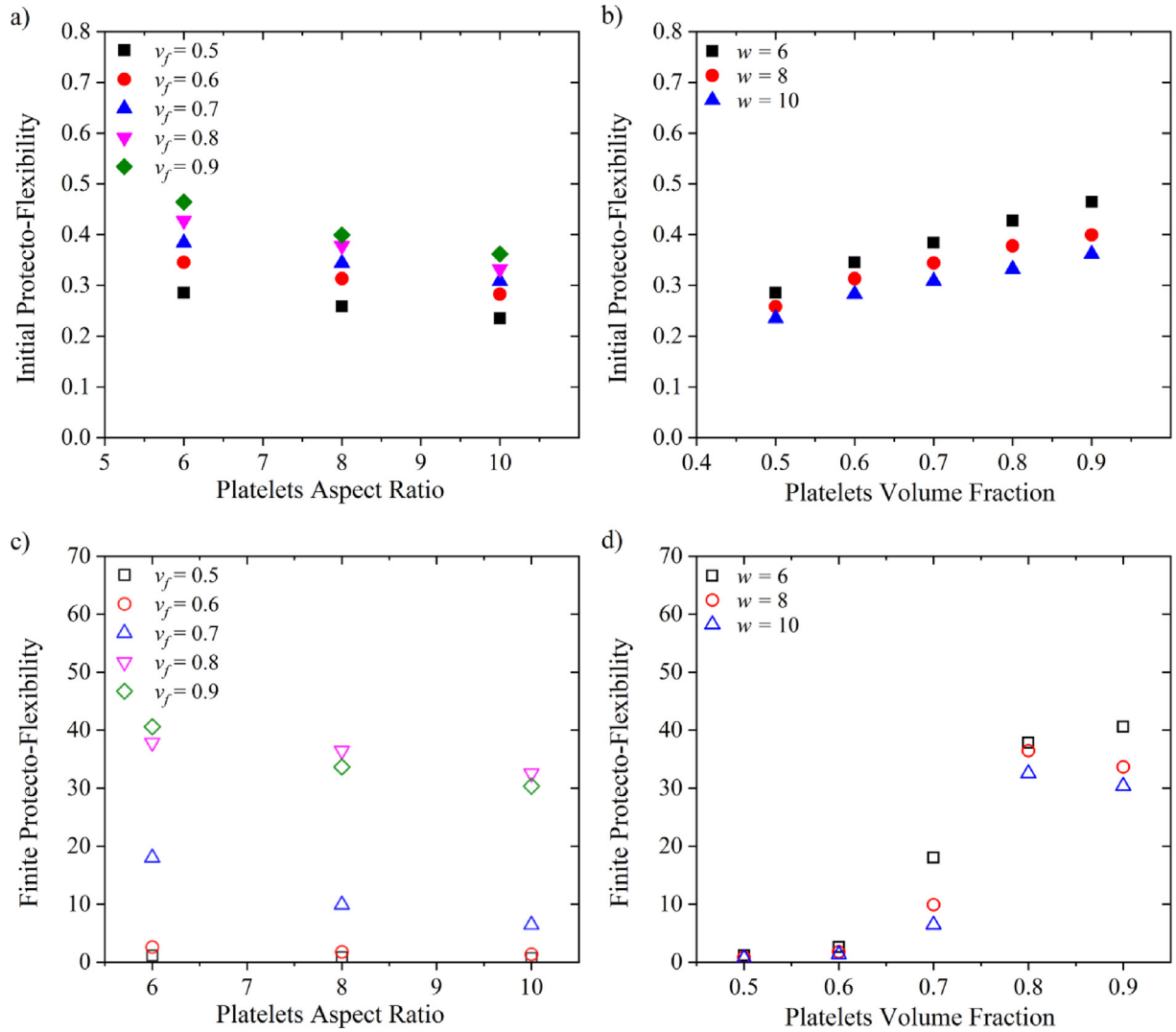


Fig. 14. Normalized indentation-to-bending stiffness ratio (protecto-flexibility) vs. platelets aspect ratio: a) initial and c) finite values. Protecto-flexibility vs. platelets volume fraction: b) initial and d) finite values.

6. Conclusions

In this work, we numerically investigate the mechanical behavior of nacre-like composite material in a large deformation context. Motivated by to design a body protective bio-inspired material architecture, we examine the competing properties: penetration resistance and flexibility. Mimicking nacre's hierarchical brick-and-mortar structure in 3D printed microstructured composite materials is an efficient approach to achieve structural materials with high mechanical performances, but the task to determine the macroscopic response of microstructured materials taking into account their microscopic nonlinear mechanical behavior usually requires a rigorous description of all microstructural details leading to impracticable computational efforts. Here, to overcome a computationally expensive full-scale modeling, a novel hybrid hierarchical/concurrent multiscale strategy is developed to evaluate the macroscopic mechanical response of nacre-like composites considering the complexity of its microstructure with reduced computational effort. The aim of the proposed technique is to adopt a hierarchical multiscale approach in domains in which the assumption of scale separation is satisfied (homogenized domains), combined with a concurrent approach in domains in which, due to strain or stress localization phenomena, this condition is no longer satisfied (fine-scale domains). In detail, fine-scale domains are characterized by a microstructural description that requires a numerical model able to completely describe

all its microscopic details and may contain heterogeneities, singularities or/and defects. Homogenized domains, instead, use information obtained by an RVE at the fine scale to describe the mechanical behavior of the homogenized material characterizing coarse-scale domains; specifically, a microscopically informed macroscopic constitutive relation in the form of macro-stress/macro-strain database previously extracted, in conjunction with an interpolation method, has been implemented in a finite element model. A comprehensive parametric analysis with respect to platelets aspect ratio and volume fraction, representing the main geometrical parameters governing the macroscopic behavior of the bio-inspired nacre-like composite material, is performed analyzing its flexibility and penetration resistance. Initially, validation and mesh convergence tests of the multiscale model were reported comparing the numerical results obtained by using multiscale and direct numerical simulations and it was deduced that using a multiscale model an amount of computational effort between 50 and 60% is saved with respect to a full-scale numerical model. Then, the flexibility is investigated by means of a three-point bending test on beams, in which the real microstructure is introduced in correspondence of the vertical concentrated load. In particular, both the initial and the finite tangent stiffness are computed as functions of aspect ratio and volume fraction. The results show that flexibility decreases with an increase in both volume fraction and aspect ratio. In detail, the investigated microstructure shows a pronounced stiffening effect for larger values of the

volume fraction, especially for the finite stiffness. On the contrary, the bending stiffness (especially the initial one) is only slightly influenced by the aspect ratio, especially for lower volume fractions (v_f ranging between 0.5 and 0.6). Moreover, the bending stiffening effect associated with the occurrence of large deformations increases for increasing values of both volume fraction and aspect ratio, and becomes negligible for low volume fractions regardless the considered aspect ratio; in fact, in this case, the bending response of the given microstructure remains almost linear. Next, the penetration resistance was investigated by employing an indentation test on a rectangular sample using a spherical indenter and modeling the contact between the indenter and the sample. The results show that the indentation load levels increase with an increase in the stiff phase volume fraction, while the aspect ratio provides a small influence on the indentation load levels. The penetration stiffness increases with increasing indentation depth, and high volume fractions and low aspect ratio offer the greatest penetration resistance, with the exception of the greatest tested volume fraction ($v_f = 0.9$), for which the highest penetration resistance is reached for the highest tested aspect ratio ($w = 10$). The influence of the stiff phase volume fraction and the platelets aspect ratio on the material resistance against indentation is further analyzed by plotting the initial and the finite tangent penetration stiffness as functions of these parameters. The finite penetration stiffness is higher than the initial value, reflecting the nonlinear behavior due to a combination of geometrical and material nonlinearity, mostly for high values of volume fraction. Both initial and finite penetration stiffness increases with an increase in volume fraction, with stiffness increase more prominent in the range of high volume fractions. On the other hand, the aspect ratio provides only a relatively small influence on the penetration stiffness, with a negligible influence on the initial values.

Next, from the comparison between the relative bending stiffness and relative penetration stiffness, it can be observed that the volume fraction strongly influences the penetration stiffness (mainly the finite value), while it slightly influences the bending stiffness. Moreover, generally speaking, an increase in penetration protection is accompanied by an increase in bending stiffness. In particular, with volume fraction values up to 0.6, the finite relative bending stiffness can be varied without affecting the finite relative penetration stiffness, which is however negligible with respect to that achieved with higher volume fractions.

These results demonstrate that the penetration resistance can be tailored as a function of the flexibility by opportunely varying inclusions volume fraction and/or aspect ratio.

Finally, the performance requirements of penetration resistance and flexibility are incorporated in a single parameter, called protecto-flexibility, which was evaluated for different values of aspect ratio and volume fraction, to investigate the role of the main microstructural parameters in this integrated measure. It is worth noting that the protecto-flexibility is very sensitive to changes in volume fraction and aspect ratio, on the contrary, the initial protecto-flexibility does not change significantly with a change in volume fraction or aspect ratio. The numerical results have shown that the finite protecto-flexibility is more important, since, generally speaking, it is two orders of magnitude greater than the initial one. This is essentially due to the delayed activation of the penetration stiffness, associated with the occurrence of large deformations.

Generally speaking, the best combinations of flexibility and penetration resistance are obtained with high volume fractions (equal or greater than 0.8), regardless of the considered aspect ratio. However, for very high aspect ratios (starting from $w = 8$) and for volume fraction values greater than 0.8, a further increase in the volume fraction inevitably leads to a reduction of the protecto-flexibility. This counter-intuitive result demonstrates that, in the presence of highly elongated platelets. A limited range of variation for the volume fraction (around the value of 0.8 for the specific staggered microstructure) guarantees the optimal coupled protection/flexibility behavior.

The reported findings can provide guidelines to enhance mechanical properties of bio-inspired nacre-like composite material manipulating the main microstructural geometry parameters. Specifically, a careful selection of volume fraction and aspect ratio can provide optimized designs to grant protection against penetration while preserving flexibility. It is worth also noting that the hybrid multiscale techniques developed in this work is reliable and can effectively be used to conduct further research on the optimization of patterns and microstructural configurations for bio-inspired structures.

Acknowledgements

Fabrizio Greco gratefully acknowledges financial support from the Italian Ministry of Education, University and Research (MIUR) under the P.R.I.N. 2017 National Grant "Multiscale Innovative Materials and Structures" (Project Code 2017J4EAYB; University of Calabria Research Unit). Stephan Rudykh gratefully acknowledges the financial support of Grainger Institute for Engineering and the University of Wisconsin Madison.

References

- [1] Xu W, Wu Y, Jia M. Elastic dependence of particle-reinforced composites on anisotropic particle geometries and reinforced/weak interphase microstructures at nano- and micro-scales. *Compos Struct* 2018;203:124–31. <https://doi.org/10.1016/j.compstruct.2018.07.009>.
- [2] Aditya Narayan D, Ben Zineb T, Polit O, Pradyumna B, Ganapathi M. Large amplitude free flexural vibrations of functionally graded graphene platelets reinforced porous composite curved beams using finite element based on trigonometric shear deformation theory. *Int J Non-Linear Mech* 2019;116:302–17. <https://doi.org/10.1016/j.nonlinmec.2019.07.010>.
- [3] Ko S, Yang J, Tuttle ME, Salviato M. Effect of the platelet size on the fracturing behavior and size effect of discontinuous fiber composite structures. *Compos Struct* 2019;227:111245. <https://doi.org/10.1016/j.compstruct.2019.111245>.
- [4] Fantuzzi N, Leonetti L, Trovalusci P, Tornabene F. Some novel numerical applications of cosserat continua. *Int J Comput Methods* 2018;15:1850054. <https://doi.org/10.1142/S0219876218500548>.
- [5] Kim Y, Jeong H, Gu GX, Ryu S. A three-dimensional fracture pattern diagram of staggered platelet structures. *Compos Struct* 2019;220:769–75. <https://doi.org/10.1016/j.compstruct.2019.04.017>.
- [6] Galich PI, Slesarenko V, Rudykh S. Shear wave propagation in finitely deformed 3D fiber-reinforced composites. *Int J Solids Struct* 2017;110–111:294–304. <https://doi.org/10.1016/j.jisols.2016.12.007>.
- [7] Le Ferrand H. Modeling the effect of microstructure on elastic wave propagation in platelet-reinforced composites and ceramics. *Compos Struct* 2019;224:111105. <https://doi.org/10.1016/j.compstruct.2019.111105>.
- [8] Zhao H, Yang Z, Guo L. Nacre-inspired composites with different macroscopic dimensions: strategies for improved mechanical performance and applications. *NPG Asia Mater* 2018;10:1–22. <https://doi.org/10.1038/s41427-018-0009-6>.
- [9] Kakisawa H, Sumitomo T. The toughening mechanism of nacre and structural materials inspired by nacre. *Sci Technol Adv Mater* 2011;12:064710. <https://doi.org/10.1088/1468-6996/12/6/064710>.
- [10] Barthelat F, Espinosa HD. An experimental investigation of deformation and fracture of nacre-mother of pearl. *Exp Mech* 2007;47:311–24. <https://doi.org/10.1007/s11340-007-9040-1>.
- [11] Ji B, Gao H. Mechanical properties of nanostructure of biological materials. *J Mech Phys Solids* 2004;52:1963–90. <https://doi.org/10.1016/j.jmps.2004.03.006>.
- [12] Ko K, Jin S, Lee SE, Lee I, Hong J-W. Bio-inspired bimaterial composites patterned using three-dimensional printing. *Compos Part B Eng* 2019;165:594–603. <https://doi.org/10.1016/j.compositesb.2019.02.008>.
- [13] Dimas LS, Buehler MJ. Modeling and additive manufacturing of bio-inspired composites with tunable fracture mechanical properties. *Soft Matter* 2014;10:4436. <https://doi.org/10.1039/c3sm52890a>.
- [14] Tran P, Ngo TD, Ghazlan A, Hui D. Bimaterial 3D printing and numerical analysis of bio-inspired composite structures under in-plane and transverse loadings. *Compos Part B Eng* 2017;108:210–23. <https://doi.org/10.1016/j.compositesb.2016.09.083>.
- [15] Kim Y, Kim Y, Libonati F, Ryu S. Designing tough isotropic structural composite using computation, 3D printing and testing. *Compos Part B Eng* 2019;167:736–45. <https://doi.org/10.1016/j.compositesb.2019.03.039>.
- [16] Rudykh S, Ortiz C, Boyce MC. Flexibility and protection by design: imbricated hybrid microstructures of bio-inspired armor. *Soft Matter* 2015;11:2547–54. <https://doi.org/10.1039/C4SM02907K>.
- [17] Slesarenko V, Volokh KY, Aboudi J, Rudykh S. Understanding the strength of bioinspired soft composites. *Int J Mech Sci* 2017;131–132:171–8. <https://doi.org/10.1016/j.jimeci.2017.06.054>.
- [18] Slesarenko V, Kazarinov N, Rudykh S. Distinct failure modes in bio-inspired 3D-printed staggered composites under non-aligned loadings. *Smart Mater Struct* 2017;26:035053. <https://doi.org/10.1088/1361-665X/aa59eb>.
- [19] Funari MF, Greco F, Lonetti P. A moving interface finite element formulation for

- layered structures. *Compos Part B Eng* 2016;96:325–37. <https://doi.org/10.1016/j.compositesb.2016.04.047>.
- [20] Greco F, Leonetti L, Lonetti P. A novel approach based on ALE and delamination fracture mechanics for multilayered composite beams. *Compos Part B Eng* 2015;78:447–58. <https://doi.org/10.1016/j.compositesb.2015.04.004>.
- [21] Triantafyllidis N, Nestorović MD, Schraad MW. Failure surfaces for finitely strained two-phase periodic solids under general in-plane loading. *J Appl Mech* 2005;73:505–15. <https://doi.org/10.1115/1.2126695>.
- [22] Bertoldi K, Boyce MC, Deschanel S, Prange SM, Mullin T. Mechanics of deformation-triggered pattern transformations and superelastic behavior in periodic elastomeric structures. *J Mech Phys Solids* 2008;56:2642–68. <https://doi.org/10.1016/j.jmps.2008.03.006>.
- [23] Li J, Slesarenko V, Rudykh S. Auxetic multiphase soft composite material design through instabilities with application for acoustic metamaterials. *Soft Matter* 2018;14:6171–80. <https://doi.org/10.1039/C8SM00874D>.
- [24] Li J, Rudykh S. Tunable microstructure transformations and auxetic behavior in 3D-printed multiphase composites: the role of inclusion distribution. *Compos Part B Eng* 2019;172:352–62. <https://doi.org/10.1016/j.compositesb.2019.05.012>.
- [25] Bruno D, Greco F, Lonetti P, Blasi PN, Sgambitterra G. An investigation on microscopic and macroscopic stability phenomena of composite solids with periodic microstructure. *Int J Solids Struct* 2010;47:2806–24. <https://doi.org/10.1016/j.ijsolstr.2010.06.013>.
- [26] Cricri G, Luciano R. Homogenised properties of composite materials in large deformations. *Compos Struct* 2013;103:9–17. <https://doi.org/10.1016/j.compstruct.2013.03.015>.
- [27] Nestorović MD, Triantafyllidis N. Onset of failure in finitely strained layered composites subjected to combined normal and shear loading. *J Mech Phys Solids* 2004;52:941–74. <https://doi.org/10.1016/j.jmps.2003.06.001>.
- [28] Slesarenko V, Rudykh S. Microscopic and macroscopic instabilities in hyperelastic fiber composites. *J Mech Phys Solids* 2017;99:471–82. <https://doi.org/10.1016/j.jmps.2016.11.002>.
- [29] Rudykh S, Bertoldi K. Stability of anisotropic magnetorheological elastomers in finite deformations: a micromechanical approach. *J Mech Phys Solids* 2013;61:949–67. <https://doi.org/10.1016/j.jmps.2012.12.008>.
- [30] Triantafyllidis N, Nestorović MD, Schraad MW. Failure surfaces for finitely strained two-phase periodic solids under general in-plane loading. *J Appl Mech* 2006;73:505. <https://doi.org/10.1115/1.2126695>.
- [31] Arora N, Batan A, Li J, Slesarenko V, Rudykh S. On the influence of inhomogeneous interphase layers on instabilities in hyperelastic composites. *Materials* 2019;12:763. <https://doi.org/10.3390/ma12050763>.
- [32] Greco F. A study of stability and bifurcation in micro-cracked periodic elastic composites including self-contact. *Int J Solids Struct* 2013;50:1646–63. <https://doi.org/10.1016/j.ijsolstr.2013.01.036>.
- [33] Greco F, Leonetti L, Luciano R, Nevone Blasi P. Effects of microfracture and contact induced instabilities on the macroscopic response of finitely deformed elastic composites. *Compos Part B Eng* 2016;107:233–53. <https://doi.org/10.1016/j.compositesb.2016.09.042>.
- [34] Rabinovitch O. Interaction, instability, and simultaneity of debonding processes in flexure of masonry walls strengthened on two sides with FRP. *Int J Fract* 2012;177:1–24. <https://doi.org/10.1007/s10704-012-9741-z>.
- [35] Greco F, Leonetti L, Medaglia CM, Penna R, Pranno A. Nonlinear compressive failure analysis of biaxially loaded fiber reinforced materials. *Compos Part B Eng* 2018;147:240–51. <https://doi.org/10.1016/j.compositesb.2018.04.006>.
- [36] Greco F, Lonetti P, Luciano R, Nevone Blasi P, Pranno A. Nonlinear effects in fracture induced failure of compressively loaded fiber reinforced composites. *Compos Struct* 2018;189:688–99. <https://doi.org/10.1016/j.compstruct.2018.01.014>.
- [37] Geymonat G, Muller S, Triantafyllidis N. Homogenization of nonlinearly elastic materials, microscopic bifurcation and macroscopic loss of rank-one convexity. *Arch Ration Mech Anal* 1993;122:231–90. <https://doi.org/10.1007/BF00380256>.
- [38] Bruno D, Greco F, Luciano R, Nevone Blasi P. Nonlinear homogenized properties of defected composite materials. *Comput Struct* 2014;134:102–11. <https://doi.org/10.1016/j.compstruc.2013.11.018>.
- [39] Miehe C, Schröder J, Becker M. Computational homogenization analysis in finite elasticity: material and structural instabilities on the micro- and macro-scales of periodic composites and their interaction. *Comput Methods Appl Mech Eng* 2002;191:4971–5005. [https://doi.org/10.1016/S0045-7825\(02\)00391-2](https://doi.org/10.1016/S0045-7825(02)00391-2).
- [40] Greco F, Luciano R. A theoretical and numerical stability analysis for composite micro-structures by using homogenization theory. *Compos Part B Eng* 2011;42:382–401. <https://doi.org/10.1016/j.compositesb.2010.12.006>.
- [41] Koley S, Mohite PM, Upadhyay CS. Boundary layer effect at the edge of fibrous composites using homogenization theory. *Compos Part B Eng* 2019;173:106815. <https://doi.org/10.1016/j.compositesb.2019.05.026>.
- [42] Leonetti L, Greco F, Trovalusci P, Luciano R, Masiani R. A multiscale damage analysis of periodic composites using a couple-stress/Cauchy multidomain model: application to masonry structures. *Compos Part B Eng* 2018;141:50–9. <https://doi.org/10.1016/j.compositesb.2017.12.025>.
- [43] Greco F, Leonetti L, Lonetti P, Nevone Blasi P. Crack propagation analysis in composite materials by using moving mesh and multiscale techniques. *Comput Struct* 2015;153:201–16. <https://doi.org/10.1016/j.compstruc.2015.03.002>.
- [44] Feo L, Greco F, Leonetti L, Luciano R. Mixed-mode fracture in lightweight aggregate concrete by using a moving mesh approach within a multiscale framework. *Compos Struct* 2015;123:88–97. <https://doi.org/10.1016/j.compstruct.2014.12.037>.
- [45] Belytschko T, Loehnert S, Song J-H. Multiscale aggregating discontinuities: a method for circumventing loss of material stability. *Int J Numer Meth Eng* 2008;73:869–94. <https://doi.org/10.1002/nme.2156>.
- [46] Greco F, Leonetti L, Luciano R, Trovalusci P. Multiscale failure analysis of periodic masonry structures with traditional and fiber-reinforced mortar joints. *Compos Part B Eng* 2017;118:75–95. <https://doi.org/10.1016/j.compositesb.2017.03.004>.
- [47] Talebi H, Silani M, Rabczuk T. Concurrent multiscale modeling of three dimensional crack and dislocation propagation. *Adv Eng Softw* 2015;80:82–92. <https://doi.org/10.1016/j.advengsoft.2014.09.016>.
- [48] Ghosh S, Bai J, Raghavan P. Concurrent multi-level model for damage evolution in microstructurally debonding composites. *Mech Mater* 2007;39:241–66. <https://doi.org/10.1016/j.mechmat.2006.05.004>.
- [49] Ogden RW. Extremum principles in non-linear elasticity and their application to composites—I. *Int J Solids Struct* 1978;14:265–82. [https://doi.org/10.1016/0020-7683\(78\)90037-9](https://doi.org/10.1016/0020-7683(78)90037-9).